AFRL-AFOSR-VA-TR-2022-0189

Image processing algorithms for imaging through atmospheric turbulence

Gilles, Jerome
SAN DIEGO STATE UNIVERSITY FOUNDATION
5250 CAMPANILE DR MC1947
SAN DIEGO, CA, 92182
USA

05/25/2022
Final Technical Report

Air Force Research Laboratory
Air Force Office of Scientific Research
Arlington, Virginia 22203
Air Force Materiel Command

REPORT DOCUMENTATION PAGE

PLEASE DO NOT RETURN YOUR FORM TO THE ABOVE ORGANIZATION.

1. REPORT DATE	2. REPORT TYPE	3. DATES COVERED	
20220525	Final	START DATE 20180301	END DATE 20220228

4. TITLE AND SUBTITLE
Image processing algorithms for imaging through atmospheric turbulence

5a. CONTRACT NUMBER	5b. GRANT NUMBER	5c. PROGRAM ELEMENT NUMBER
	FA9550-18-1-0139	61102F
5d. PROJECT NUMBER	**5e. TASK NUMBER**	**5f. WORK UNIT NUMBER**

6. AUTHOR(S)
Jerome Gilles

7. PERFORMING ORGANIZATION NAME(S) AND ADDRESS(ES)
SAN DIEGO STATE UNIVERSITY FOUNDATION
5250 CAMPANILE DR MC1947
SAN DIEGO, CA 92182
USA

8. PERFORMING ORGANIZATION REPORT NUMBER

9. SPONSORING/MONITORING AGENCY NAME(S) AND ADDRESS(ES)	10. SPONSOR/MONITOR'S ACRONYM(S)	11. SPONSOR/MONITOR'S REPORT NUMBER(S)
Air Force Office of Scientific Research 875 N. Randolph St. Room 3112 Arlington, VA 22203	AFRL/AFOSR RTB1	AFRL-AFOSR-VA-TR-2022-0189

12. DISTRIBUTION/AVAILABILITY STATEMENT
A Distribution Unlimited: PB Public Release

13. SUPPLEMENTARY NOTES

14. ABSTRACT
In this grant, we aimed at studying image processing algorithms for turbulence mitigation related problems. This grant was the continuation of our previous grant (FA9550-15-1-0065). We developed an original approach, called BATUD (Blind Atmospheric TUrbulence Deconvolution), to perform atmospheric deblurring. We created two datasets, OTIS and SOTIS, that we made publicly available. The first one is a small dataset containing real static and dynamic (i.e. with a moving target) sequences. The second one is a very large dataset created thanks to an atmospheric turbulence simulator. The purpose of such dataset is twofold: 1) to run extensive algorithm performance evaluations (we have run the evaluation of unsupervised algorithms during this project); 2) to develop dedicated neural network based techniques in a near future. We also investigated the use of empirical wavelets to perform deblurring tasks which led to a self-adapting algorithm.

15. SUBJECT TERMS

16. SECURITY CLASSIFICATION OF:			17. LIMITATION OF ABSTRACT	18. NUMBER OF PAGES
a. REPORT U	b. ABSTRACT U	c. THIS PAGE U	UU	15

19a. NAME OF RESPONSIBLE PERSON	19b. PHONE NUMBER *(Include area code)*
ARJE NACHMAN	426-8427

AFOSR Final Performance Report

Project title: Image Processing Algorithms

Award Number: FA9550-18-1-0139

Start Date: March 1st, 2018
End Date: Feb. 28th, 2022

Project Manager: Dr. Arje Nachman
Program Officer, Electromagnetics
875 North Randolph Road
Ste 325, Room 3112
Arlington, VA 22203
Phone: 703-696-8427
FAX: 703-696-8450
Email: arje.nachman@us.af.mil

Principal Investigator: Prof. Jérôme Gilles
Department of Mathematics & Statistics
San Diego State University
5500 Campanile Dr
San Diego, CA, 92182-7720
Phone: 619-594-7240
FAX: 619-594-6746
Email: jgilles@sdsu.edu

1 Introduction

In this grant, we aimed at studying image processing algorithms for turbulence mitigation related problems. This grant was the continuation of our previous grant (FA9550-15-1-0065). We developed an original approach, called BATUD (Blind Atmospheric TUrbulence Deconvolution), to perform atmospheric deblurring. We created two datasets, OTIS and SOTIS, that we made publicly available. The first one is a small dataset containing real static and dynamic (i.e. with a moving target) sequences. The second one is a very large dataset created thanks to an atmospheric turbulence simulator. The purpose of such dataset is twofold: 1) to run extensive algorithm performance evaluations (we have run the evaluation of unsupervised algorithms during this project); 2) to develop dedicated neural network based techniques in a near future. We also investigated the use of empirical wavelets to perform deblurring tasks which led to a self-adapting algorithm.

2 Accomplishments

2.1 Blind Atmospheric TUrbulence Deconvolution (BATUD)

We have investigated a new way to re-formulate the deconvolution algorithm based on the Fried kernel we originally proposed in [11]. The main issue in this formulation is the presence of four physical parameters. In particular the C_n^2 parameter, corresponding to the turbulence strength, is very hard to estimate. A brute force approach has been proposed in [11], but it is computationally very expensive and not implementable in real-time systems. To circumvent this issue, we proposed a new formulation for the blurring kernel which depends only on two parameters that can easily be estimated. Our new kernel is defined in the Fourier domain by

$$M_{\mathbf{a}}(\omega) = A(\omega) \exp\left\{ \sum_{i=1}^{N} a_i f_i(\omega) \right\}, \tag{1}$$

where $N \in \mathbb{N}$, $A : \mathbb{R}^+ \to \mathbb{R}$ and $f_i : \mathbb{R}^+ \to \mathbb{R}$ are fixed and known while $\mathbf{a} = (a_1, \ldots, a_N)^T$ is a set of parameters to be estimated. We can notice that this kernel corresponds to the Fried kernel if we choose (hereafter the notation $a \asymp b$ mean "a plays the role of b")

$$\begin{gathered} A(\omega) = M_0(\omega), \quad N = 2, \\ a_1 \asymp (2.1X)^{5/3}, \quad a_2 \asymp (2.1X)^{5/3} V(Q, X), \\ f_1(.) = -(\cdot)^{5/3} \quad \text{and} \quad f_2(.) = (\cdot)^2, \end{gathered} \tag{2}$$

where M_0, corresponds to a combination of the optical system + atmosphere modulation transfer functions when the turbulence is negligible (see [11] for details).
Note that this model also encompasses other types of kernel like the traditional Gaussian kernel of bandwidth γ by choosing $A(\omega) = 1, N = 1, a_1 = \gamma^2/2$ and $f_1(\cdot) = -(\cdot)^2$.
Equipped with this kernel, we define the image formation model by

$$y(\omega) = M_{\mathbf{a}}(\omega) \cdot x(\omega) + \varepsilon(\omega), \tag{3}$$

where $M_{\mathbf{a}}$ is the unknown underlying Fried kernel, x the spectrum of the underlying clean image and ε is the spectrum of an additive white Gaussian noise component with standard deviation $\sigma > 0$. Then the deconvolution is performed by solving, for $\alpha > 0$,

$$\underset{x, \mathbf{a}, \lambda}{\operatorname{argmin}} \; \tfrac{1}{2\sigma^2} \left\| y - M_{\mathbf{a}} \cdot x \right\|_2^2 + R(x) + \lambda \| M_{\mathbf{a}} \|_2^2 + \frac{\alpha^2}{\lambda} \, . \tag{4}$$

The first term in (4) is the standard ℓ_2^2 data fidelity term that typically results from a Bayesian perspective when assuming that the noise component is additive white Gaussian with standard deviation σ. The second term, $R(x) \geqslant 0$, is a regularization term enforcing $x^\star$ to fit some image prior knowledge. We considered an image regularization term based on a zero-mean Gaussian Mixture Model (GMM) prior of natural image patches. The terms $\lambda \|M_{\mathbf{a}}\|_2^2$ and $\frac{\alpha^2}{\lambda}$ are used to guarantee the stability of the algorithm. The corresponding algorithm steps are described by

$$x^{t+1} \in \underset{x}{\operatorname{argmin}} \tfrac{1}{2\sigma^2} \|y - M_{\mathbf{a}^t} \cdot x\|_2^2 + R(x), \tag{5}$$

$$\lambda^{t+1} \in \underset{\lambda}{\operatorname{argmin}} \lambda \|M_{\mathbf{a}^t}\|_2^2 + \frac{\alpha^2}{\lambda}, \tag{6}$$

$$\mathbf{a}^{t+1} \in \underset{\mathbf{a}}{\operatorname{argmin}} \tfrac{1}{2\sigma^2} \left\|y - M_{\mathbf{a}} \cdot x^{t+1}\right\|_2^2 + \lambda^{t+1} \|M_{\mathbf{a}}\|_2^2, \tag{7}$$

where $t \geqslant 0$ is the time step. The initialization of the different variables is discussed in [11].

Problem (5) is a non-blind deconvolution problem we solve using the FEPLL algorithm [19]. Problem (6) has a trivial closed form solution, and problem (7) can be easily minimized using a Newton's descent approach.

In this report, we only illustrate a few experimental results, please see [11] for more experiments. Figures 1 and 2 show the deconvolution results on simulated blur and real atmospheric turbulence blur (after the input sequences have been stabilized). The algorithm shows excellent results. In the article, we show that the estimated kernels, in the simulated scenarios, match almost perfectly the artificially ones used to create the blurry images. In [11], we also perform comparisons with state of the art unsupervised blind deconvolution algorithms and show that BATUD outperforms all of them.

2.2 Empirical wavelet based deconvolution

Within the last eight years, the P.I. has developed a new type of wavelets, called empirical wavelets (EW). The particularity of these wavelets lies in the fact that they are adaptive wavelets (i.e. data driven). The purpose of the empirical wavelet transform is to extract harmonic modes (i.e. amplitude modulated/frequency modulated components) from any original signal or image. To achieve such adaptability, the supports of the expected harmonic modes are detected within the Fourier domain, then one wavelet filter is built with each respective support, providing us a wavelet filter-bank $\{\phi_1(t), \{\psi_n(t)\}_{n=1}^N\}$. In 2D, we have proposed to use several geometrical constraints leading to tensor, Littlewood-Paley, and curvelets types of EW, as well as a fully unconstrained type of EW, called empirical watershed wavelets. See [2, 6, 7, 9, 10] for more detailed descriptions of these empirical wavelets families and their properties.

Since algorithms promoting sparsity in the wavelet domain have been widely used in the literature for image restoration, and more particularly image deconvolution, we investigated the use of these empirical wavelets for such purpose and evaluated their potential. The corresponding mathematical model is given by

$$\min_u ||Du||_1 + \frac{\lambda}{2}||A * u - f||_2^2, \tag{8}$$

where λ is a regularization parameter, D is the wavelet transform operator, A the blur kernel, and f the blurry image. Such minimization problem can efficiently be solved by a primal-dual optimization technique which leads to an iterative algorithm. The adaptability of the empirical wavelets opens two options: 1) we keep the family of empirical wavelets (built during the initialization) fixed during all iterations, 2) we update the family of empirical wavelets at each iteration. This basically means that the deconvolution algorithm adapts itself to not only the input blurry image, but also its deblurring capabilities. These two approaches are summarized by Algorithms 1 and 2.

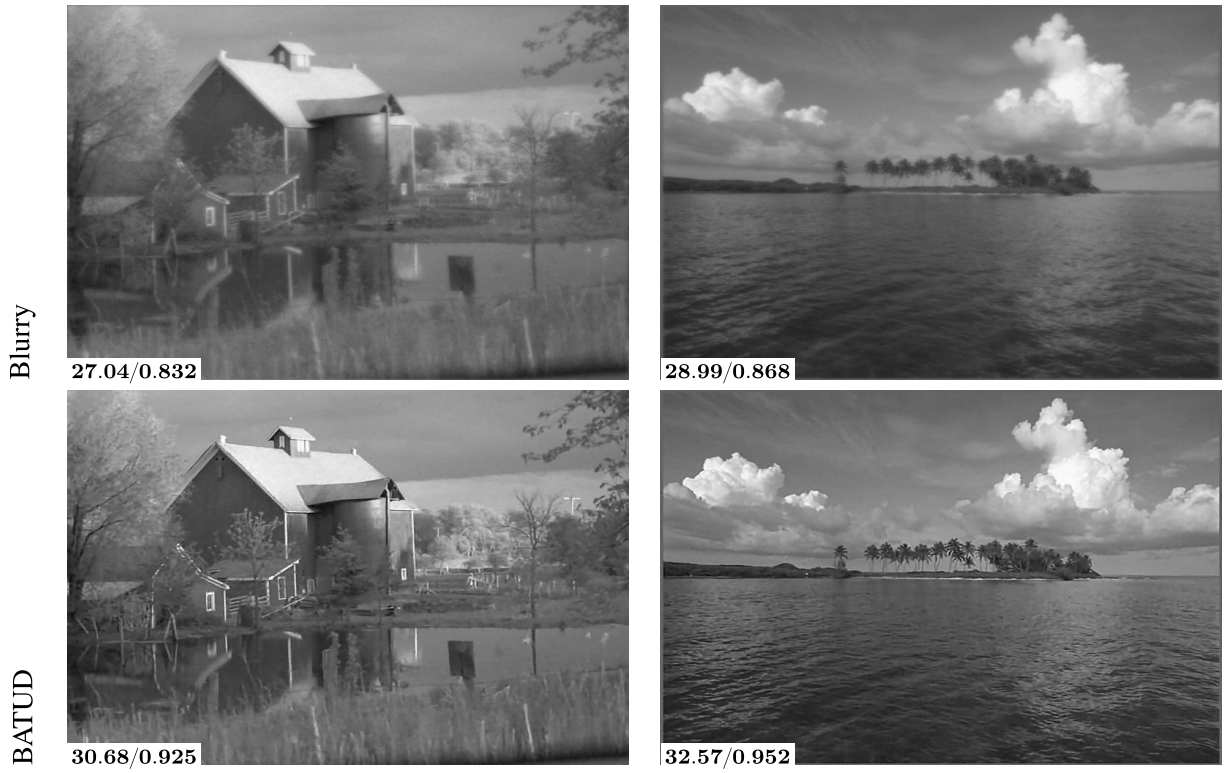

Figure 1: BATUD results on different simulated scenarios of blur and noise from the Kodak dataset. PSNR (left) and SSIM (right) values are displayed on the bottom-left.

Algorithm 1 Empirical wavelet based deconvolution with a kept fixed set of filters.

Input: Choose $\nu, \sigma > 0; \theta \in \{0, 1\}; u^0 = \tilde{u}^0 = f;$

Build the set of empirical wavelet filters, $\{\widehat{\varphi_n}\}$ based on the magnitude spectrum of f. This defines the operator D_ϵ^0

Initialize $y^0 = D_\epsilon^0 f, k = 0$

while Convergence criteria not met **do**

$y_{i,j}^{k+1} = \frac{y_{i,j}^k + \sigma(D_\epsilon^0 \tilde{u}^k)_{i,j}}{\max(1, |y_{i,j}^k + \sigma D_\epsilon^0 \tilde{u}^k)_{i,j}|)}$

$u^{k+1} = \left((\widehat{I} + \nu\lambda|\widehat{A}|^2)^{-1} (\nu\lambda\overline{\widehat{A}}\widehat{f} + \widehat{u}^k - \nu(\widehat{D_\epsilon^0)^{-1} y^{k+1}}) \right)^\vee$

$\tilde{u}^{k+1} = u^{k+1} + \theta(u^{k+1} - u^k)$

$k = k + 1$

end while

Output: Numerical solution u of $\min_u ||D_\epsilon^0 u||_1 + \frac{\lambda}{2}||Au - f||_2^2$.

Figure 2: Results obtained on two images with real atmospheric turbulence.

Algorithm 2 Empirical wavelet based deconvolution with sets of wavelet filters that are updated at each iteration.

Input: Choose $\nu, \sigma > 0; \theta \in \{0, 1\}; u^0 = \tilde{u}^0 = y = f;$

Initialize the set of empirical wavelet filters, $\{\widehat{\varphi_n^k}\}$ based on the magnitude spectrum of f.

$k = 0$

while Convergence criteria not met **do**

$y_{i,j}^{k+1} = (D_\epsilon^k)^{-1} \frac{D_\epsilon^k y_{i,j}^k + \sigma (D_\epsilon^k \tilde{u}^k)_{i,j}}{\max(1, |D_\epsilon^k y_{i,j}^k + \sigma D_\epsilon^k \tilde{u}^k)_{i,j}|)}$

$u^{k+1} = \left((\widehat{I} + \nu\lambda |\widehat{A}|^2)^{-1} (\nu\lambda \overline{\widehat{A}} \widehat{f} + \widehat{u}^k - \nu \widehat{y}^{k+1}) \right)^\vee$

$\tilde{u}^{k+1} = u^{k+1} + \theta(u^{k+1} - u^k)$

Update the set of empirical filter $\{\widehat{\varphi_n^k}\}$ based on the magnitude spectrum of u^{k+1}

$k = k + 1$

end while

Output: Numerical solution u.

An example of the obtained results is illustrated in Figure 3 and more are available in [2]. Our experiments show that empirical wavelets do perform equally with classic wavelets in the case of non-textured

images. However, the empirical wavelets clearly outperform classic wavelets in the case of textured images (which is considered as one of the hardest type of images to restore). This could potentially have interesting applications in the observation/surveillance of area with a lot of vegetation, or the identification of camouflaged targets.

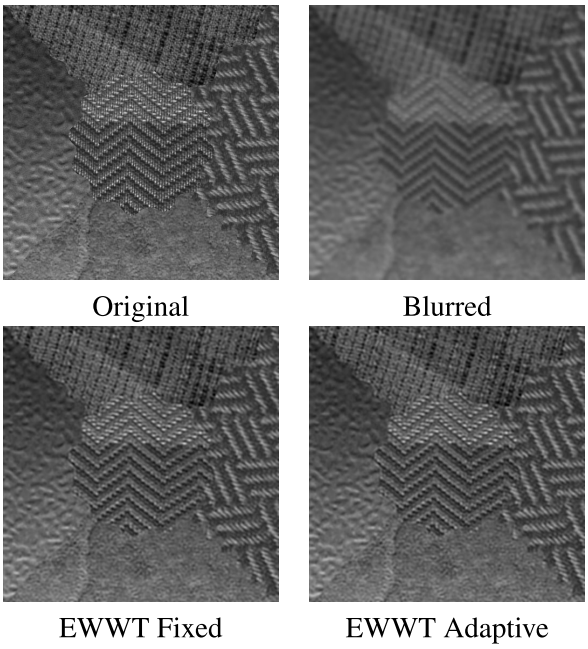

Figure 3: Example of a deconvolution performed on an image with a blur variance of $\sigma_B^2 = 3$ using both a fixed or adaptive set of filters with the empirical watershed wavelet transform.

2.3 Detection of moving targets through atmospheric turbulence from a non-stationary imaging system

In our previous work, [8], we have shown that targets moving through atmospheric turbulence could be easily detected by decomposing the optical flow information. The idea is to separate, in the space-time domain, the movement vector fields corresponding to homogeneous trajectories (created by the expected moving targets) and the oscillatory/random movements (created by the turbulence). To achieve such separation, we modified the so-called "cartoon + textures" image decomposition techniques to work on space-time vector fields using spaces of curvelet functions. However, our approach assumed that the imaging system was stationary, assumption which is not always fulfilled in practice (for instance for a system embedded on a moving platform).

To avoid this problem, we have developed a model of the impact of non-stationary movement on the space-time vector field $\mathbf{V} = (V_x, V_y)$. A pinhole camera model [22] was used to derive the relation between real world coordinates $(\mathcal{X}, \mathcal{Y}, \mathcal{Z})$ and the pixel coordinates (x, y):

$$\begin{aligned} V_x &= \frac{T_z x - T_x \mathfrak{f}}{\mathcal{Z}} + \omega_x \frac{xy}{\mathfrak{f}} - \omega_y \left(\mathfrak{f} + \frac{x^2}{\mathfrak{f}} \right) + \omega_z y \\ V_y &= \frac{T_z y - T_y \mathfrak{f}}{\mathcal{Z}} + \omega_x \left(\mathfrak{f} + \frac{y^2}{\mathfrak{f}} \right) - \omega_y \frac{xy}{\mathfrak{f}} - \omega_z x \end{aligned} \tag{9}$$

where $\mathfrak{f}$ is the focal length, $T_{(x,y,z)}$ and $\omega_{(x,y,z)}$ correspond to translation and rotation movement in the x, y, z

direction. After some calculation (see [17] for full details), we got the estimates

$$\omega_z = \frac{-1}{2}\langle(\nabla \times \mathbf{V}) \cdot \hat{\mathbf{k}}\rangle, \tag{10}$$

$$\begin{aligned}\frac{\omega_x}{\mathfrak{f}} &= -\left\langle \partial_x \left((\nabla \times \mathbf{V}) \cdot \hat{\mathbf{k}}\right)\right\rangle \\ \frac{\omega_y}{\mathfrak{f}} &= -\left\langle \partial_y \left((\nabla \times \mathbf{V}) \cdot \hat{\mathbf{k}}\right)\right\rangle,\end{aligned} \tag{11}$$

$$\begin{aligned}\frac{T_x\mathfrak{f}}{\mathcal{Z}} &= -\langle V_x^T\rangle = \left\langle -\frac{\omega_y}{\mathfrak{f}}\left(\mathfrak{f}^2 + x^2\right)\right\rangle - \langle V_x\rangle \\ \frac{T_y\mathfrak{f}}{\mathcal{Z}} &= -\langle V_y^T\rangle = \left\langle \frac{\omega_x}{\mathfrak{f}}\left(\mathfrak{f}^2 + y^2\right)\right\rangle - \langle V_y\rangle,\end{aligned} \tag{12}$$

and

$$\frac{T_z}{\mathcal{Z}} = \frac{1}{2}\langle \nabla \cdot \mathbf{V}\rangle. \tag{13}$$

The following algorithm described the global motion compensation technique which is applied as a preprocessing before performing the vector field decomposition described above as depicted in Figure 4. We have tested a simple target detection algorithm with and without the global motion compensation, and we have found that removing the global movement can drastically improve the detection performances.

Algorithm 3 Pseudo code corresponding to the analytical compensation model

1: Inputs: flow to decompose $\mathbf{V}$, focal length $\mathfrak{f}$
2: Smooth V_x and V_y with a Gaussian filter
3: Compute ω_z via equation (10), and $\omega_{x,y}$ via (11)
4: Using values $\frac{\omega_{x,y}}{\mathfrak{f}}$ compute $\frac{T_{x,y}\mathfrak{f}}{\mathcal{Z}}$ via (12)
5: Compute $\frac{T_z}{\mathcal{Z}}$ via (13)
6: Substitute the computed components into equation (9) to produce the approximated global motion flow $\mathbf{M}$.
7: Compute compensated optical flow $\mathbf{V}_c = \mathbf{V} - \mathbf{M}$
8: **return** $\mathbf{V}_c$

2.4 Turbulence image datasets and algorithmic performance evaluation

Given the vast literature on turbulence mitigation (we referenced about one hundred papers), it becomes imperative to have some common algorithmic performance evaluation methodology. This implies to not only define some metrics, but also to have a substantial amount of data to perform such evaluation. Unfortunately, such dataset is not available today. The following sections describe our contributions to this topic.

2.4.1 Open Turbulence Image Set (OTIS)

Thanks to an internal small grant, we bought a modified GoPro camera with interchangeable lenses. Taking advantage of the turbulence created close to the artificial turf ground on the campus practice fields, we acquired some sequences of both static and dynamic (i.e. with a moving target) scenes. Their characteristics are summarized in Table 1 and 2, while Figures 5 and 6 illustrate some images with their groundtruths.

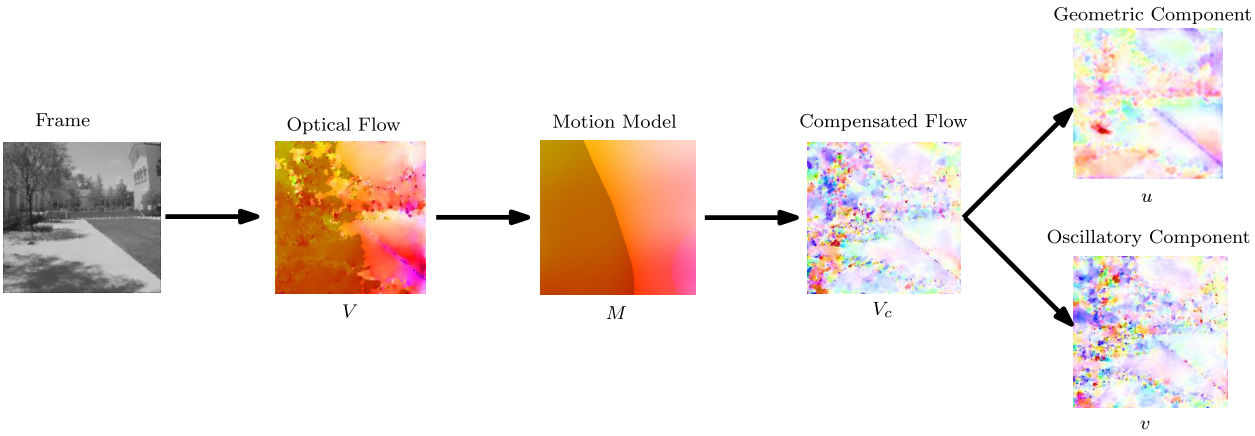

Figure 4: Overall steps in decomposing the movement vector field with global motion compensation.

Table 1: Summary of the different static sequences in OTIS

Folder Name	**Sequence Name**	**Number of images**	**Image size**	**Turbulence level**	**Ground Truth**
Fixed Background	Door	300	520x520	Strong	No
Fixed Patterns	Pattern1	64	302x309	Weak	Yes
	Pattern2	64	291x287	Weak	Yes
	Pattern3	300	113x117	Strong	Yes
	Pattern4	300	109x113	Strong	Yes
	Pattern5	300	113x117	Strong	Yes
	Pattern6	300	109x113	Strong	Yes
	Pattern7	300	122x125	Strong	Yes
	Pattern8	300	119x122	Strong	Yes
	Pattern9	300	152x157	Medium	Yes
	Pattern10	300	149x149	Medium	Yes
	Pattern11	300	172x183	Medium	Yes
	Pattern12	300	172x173	Medium	Yes
	Pattern13	300	202x202	Weak	Yes
	Pattern14	300	196x193	Weak	Yes
	Pattern15	300	134x139	Strong	Yes
	Pattern16	300	135x135	Strong	Yes

2.4.2 Simulated Open Turbulence Image Set (SOTIS)

If the previously described OTIS dataset is useful for basic development and testing, it is not large enough to run conclusive performance evaluations. Moreover, with the recent developments of neural networks for image restoration purposes, (very) large datasets are needed to train such algorithms. However, acquiring such large dataset in the field is very expensive and complicated since we can't control the turbulence strength in the real atmosphere. To overcome these issues, we decided to create sequences using a simulation algorithm. We used the recent algorithm proposed by Chimitt et al. [4] which takes into account the

Table 2: Summary of the different dynamic sequences in OTIS

Folder Name	**Sequence Name**	**Number of images**	**Image size**	**Turbulence level**	**Ground Truth**
Moving Target	Car1	100	200x200	Medium	Yes
	Car2	315	500x200	Medium	Yes
	Car3	51	300x300	Medium	Yes
	Car4	101	300x300	Medium	Yes

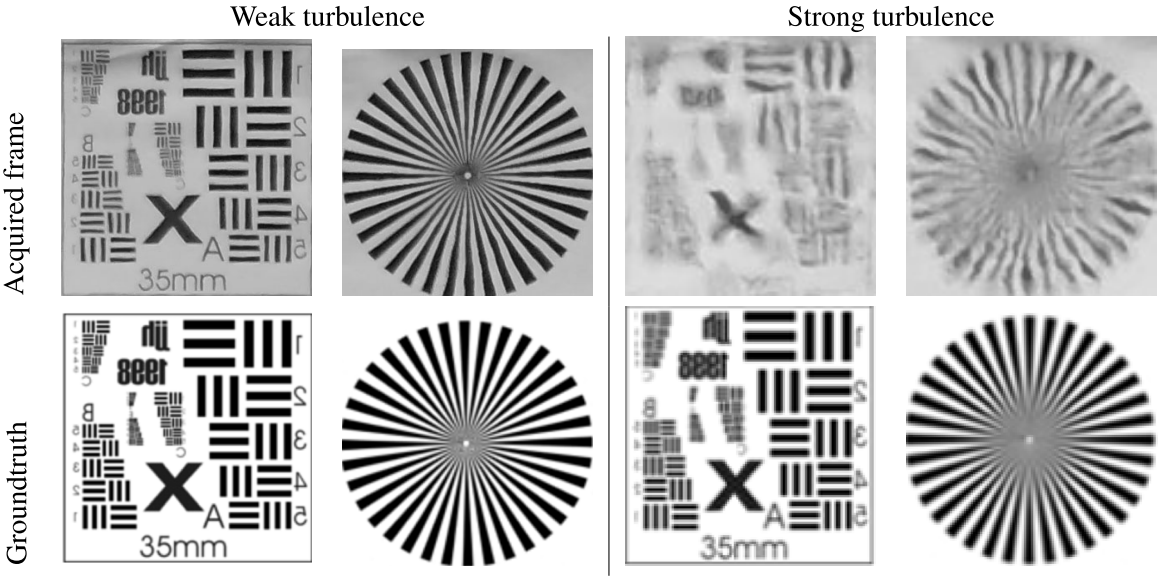

Figure 5: Samples of frames from OTIS from different fixed pattern sequences and their corresponding groundtruths.

different physical aspects of turbulence. We modified the shared MATLAB code [1] from the authors of [4], to parallelize it for speeding up purposes.

To guarantee enough variability in our dataset (i.e. images containing buildings, pedestrians, vehicles, vegetation, signs,...), we cropped 215 images of size 256×256 pixels to serve as ground-truth images from the Eurasian-Cities dataset [21]. The simulator main parameters are: the focal length $d = 0.3$, the aperture diameter $D = 0.054$ (we kept these values to the default ones given by the authors of [4]), the distance sensor-scene L, the refractive index C_n^2. To create a wide range of turbulence and observation scenarios, we sampled L and C_n^2 as follows: $L = 1, 2, 3, 4$ km, $C_n^2 = a^{-b}$ where $a = 1, 3, 5, 7, 9$ and $b = 14, 15, 16, 17$. We fix the number of frames in the generated sequences to $N = 50$. These choices lead to the creation of 80 sequences for each ground-truth, resulting in a total of 17400 sequences in SOTIS. Figure 7, illustrates some frame examples from the available sequences in both weak and strong turbulence cases.

[1] `https://engineering.purdue.edu/ChanGroup/index.html`

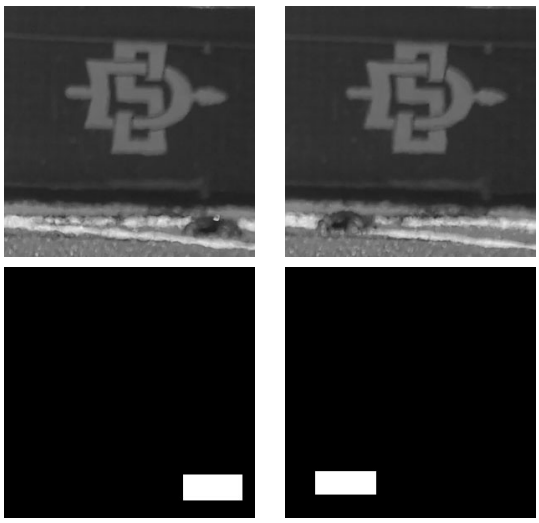

Figure 6: Frames 16 and 34 from a dynamic sequence (top) and their corresponding groundtruths frames (bottom) from OTIS.

2.4.3 Performance evaluation

Using the SOTIS dataset, we can run different types of performance evaluation. We focused on the evaluation of turbulence mitigation algorithms. Such algorithms are usually made of two main steps (the input being a sequence of images): 1) a stabilization step which purpose is to correct geometric distortions, 2) a deblurring step. Note that a few algorithms combining these two steps together do exist in the literature. We used the stabilization algorithm proposed in [14] which combines optical flow (either the Lukas-Kannade or $TV - L^1$ versions) and some regularization term (either total variation, TV, or nonlocal TV), as well as a simple temporal average. Regarding the deblurring step, we only investigated unsupervised algorithms.

The tested unsupervised deblurring techniques were BATUD [5], CLS (framelet based deconvolution) [3], and ZWZ ($\ell^2 - \ell^p$ sparse prior based variational model) [23]. We also tested the wavelet fusion based algorithm proposed by [1], denoted ATM, and the lucky imaging approach developed in [15], denoted IRAT. These last two algorithms are combined approaches, i.e they have their own stabilization and deconvolution approaches.

Since SOTIS provides the ground-truths images (which will be denoted f_{gt} hereafter), we propose to measure performances by using the widely accepted peak signal to noise ratio (PSNR) and structural similarity index measure (SSIM) metrics, respectively defined by (we denote f_{rest} the restored image):

$$PSNR(f_{gt}, f_{rest}) = 10 \log_{10} \left(\frac{\max_{im}}{\|f_{gt} - f_{rest}\|_2^2} \right),$$

where $\max_{im}$ is the maximum value an image can reach (255 for 8-bits encoded images); and

$$SSIM(f_{gt}, f_{rest}) = \frac{(2\mu_{gt}\mu_{rest} + c_1)(2\sigma_{gt,rest} + c_2)}{(\mu_{gt}^2 + \mu_{rest}^2 + c_1)(\sigma_{gt}^2 + \sigma_{rest}^2 + c_2)},$$

where μ_{gt} and μ_{rest} are respectively the average of f_{gt} and f_{rest}; $\sigma_{gt}, \sigma_{rest}, \sigma_{gt,rest}$ their variances and covariance, c_1, c_2 two constants defined from the images dynamic range. Notice that the SSIM metric provides values in the range $[0, 1]$ (1 being the best performance).
With the SOTIS dataset, we provide several MATLAB scripts where the user can easily plug any stabilization, deblurring or combined algorithms and create the appropriate directory structure to store his results. We

Figure 7: Examples of available sequences in the SOTIS dataset. The used ground-truth images are given in the left column. The corresponding weak and strong turbulence scenarios are illustrated in the center and right columns, respectively.

also provide a script that parses all the results and build a CSV file that contains the corresponding PSNR and SSIM values. Any statistical software, like R, can then extract all the useful evaluation statistics. Figures 8 and 9 provide the obtained performances results. As expected, these results show that the performances decrease with respect to both the distance and turbulence strength. An interesting preliminary observation is the fact that a stabilization performed by a basic temporal average seems to provide similar performances compared to more advanced stabilization. This could be explained by the fact that deconvolution algorithms have made a lot of improvement these last decades and seem less sensitive on the stabilization step. This could potentially be a good news since a temporal average is very easy to implement and runs in real time.

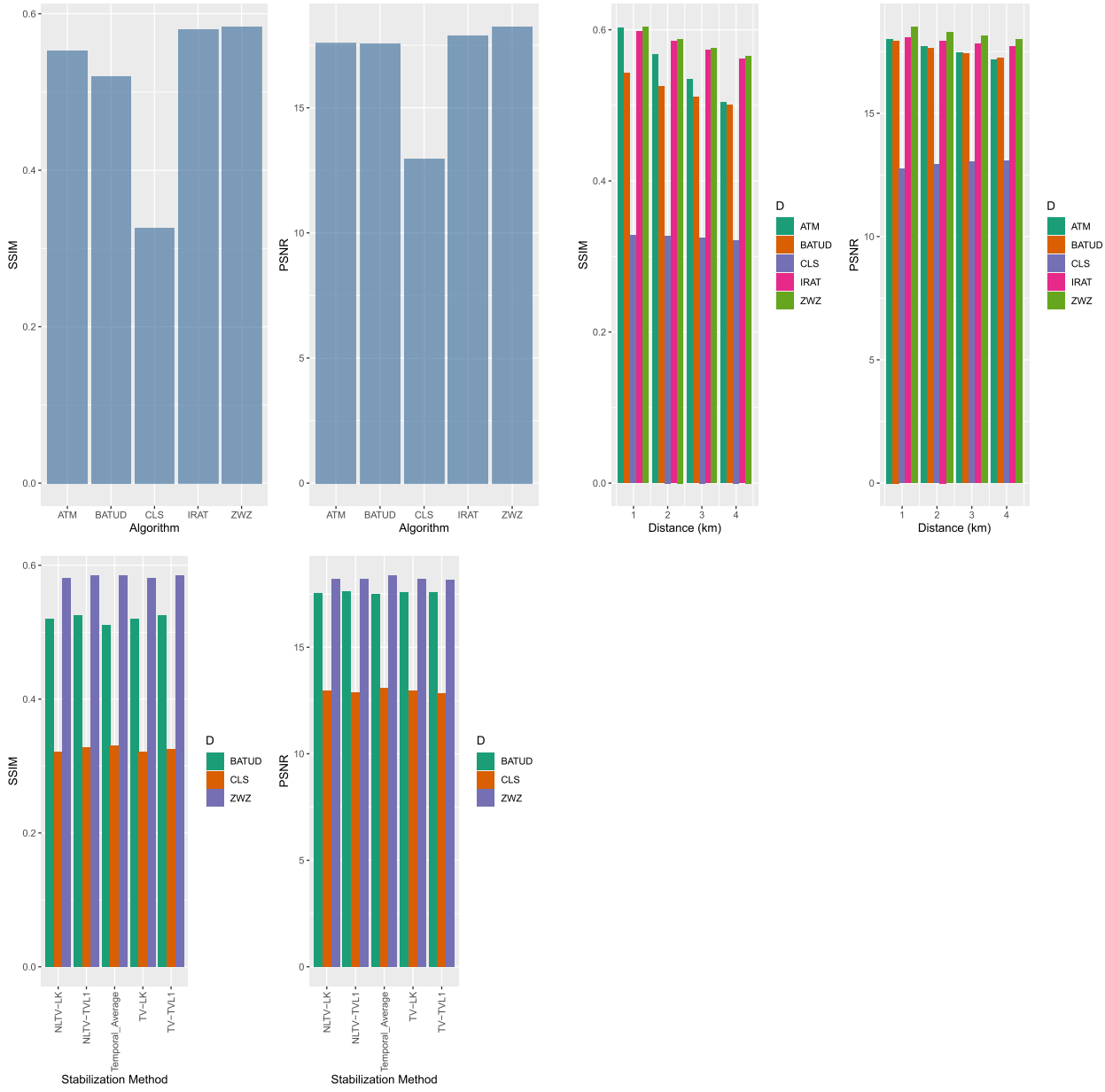

Figure 8: Performances results for unsupervised algorithms. Top left: overall average performances, top-right: average performances with respect distance, bottom-left: average performance with respect the stabilization.

3 Impacts

The works done during this project has led to several publications impacting the community working on atmospheric turbulence related image processing algorithms:

- J.Gilles, N.B.Ferrante, "Open Turbulent Image Set (OTIS)", Pattern Recognition Letters, Vol.86, 38–41, 2017.
- J.Gilles, F.Alvarez, N.B.Ferrante, M.Fortman, L.Tahir, A.Tarter, A.von Seeger, "Detection of moving

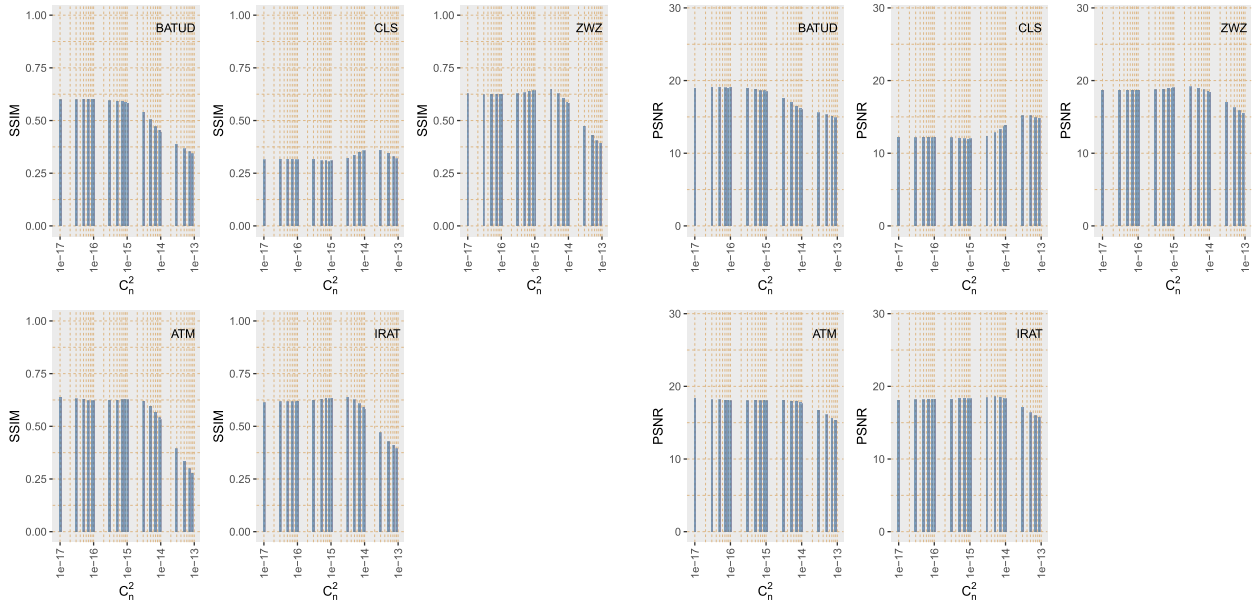

Figure 9: Performances results for unsupervised algorithms with respect turbulence strength (C_n^2), SSIM on left, PSNR on right.

objects through turbulent media. Decomposition of Oscillatory vs Non-Oscillatory spatio-temporal vector fields", Image and Vision Computing Journal, Vol.73, 40–55, May 2018.

- N.B.Ferrante, S.Parameswaran, J.Gilles, "Investigation of moving objects through atmospheric turbulence from a non-stationary platform", Proceedings of the SPIE 11137, Applications of Digital Image Processing XLII, 111370X, San Diego, August 2019.
- B.Hurat, Z.Alvarado, J.Gilles. "The Empirical Watershed Wavelet", Journal of Imaging, Special Issue "2020 Selected Papers from Journal of Imaging Editorial Board Members", Vol.6, No.12, 140, 2020.
- C-A.Deledalle, J.Gilles, "Blind Atmospheric TUrbulence Deconvolution", IET Image Processing, Vol.14, No.14, 3422–3432, 2020.
- T.Jain, M.Lubien, J.Gilles. "Evaluation of neural network algorithms for atmospheric turbulence mitigation", SPIE Defense & Commercial Sensing Conference, Orlando, Florida, USA, April 2022.

The scientific impacts can be summarized as:

1. from the theoretical perspective: our generalization of the image decomposition models to vector fields decompositions, and our study of empirical wavelets,
2. from the algorithmic perspective: by the development of our unique approach for atmospheric deconvolution,
3. from a practical point of view: by the creation of the OTIS and SOTIS datasets which will help the community to develop, train and evaluate turbulence mitigation algorithms.

This project has also impacted many students both at the undergraduate and graduate levels, and who ended up being co-authors of the above listed articles. M. Fortman, L. Tahir, A. Tarter and A. von Seeger were undergraduate students when they worked with me and all decided to continue their academic journey in

both master or Ph.D programs. F. Alvarez, N.B. Ferrante, B. Hurat, Z. Alvarado, T. Jain, M. Lubien were graduate students and their contributions to this project were their master thesis work. Several of them have since found scientist positions at the Naval Information Warfare Center Pacific (NIWC), the Lawrence Livermore National Laboratory, Facebook, GraphWear Technologies Inc.

4 Future work

If the OTIS dataset is already available online, the SOTIS dataset is too big to be hosted on classic platforms. We are currently looking for a long-term solution to host that dataset to make it publicly available (today it can be requested by contacting the P.I.). It would also be valuable for the community to design a website that will capitalize the performance results and where any other research teams could contribute.

We started to investigate the use of supervised (i.e. neural networks) algorithms to perform turbulence mitigation. In particular, we started to test some existing deep learning based deblurring techniques. Our preliminary results seem to indicate that they perform better than unsupervised algorithms.

We are also planning to continue our investigations, both theoretical and practical, about empirical wavelets. The theoretical explorations are needed to better understand the "adaptability" of such wavelets and what we can expect from it from a practical point of view. We also believe empirical wavelets have a close tie with neural networks and we want to unveil these connections.

References

[1] Nantheera Anantrasirichai, Alin Achim, Nick G. Kingsbury, and David R. Bull. Atmospheric turbulence mitigation using complex wavelet-based fusion. *IEEE Transaction in Image Processing*, 22(6):2398–2408, June 2013.

[2] B.Hurat, Z.Alvarado, and J.Gilles. The Empirical Watershed Wavelet. *Journal of Imaging*, 6(12):140, 2020.

[3] Jian-Feng Cai, Hui Ji, Chaoqiang Liu, and Zuowei Shen. Framelet-based blind motion deblurring from a single image. *IEEE Transactions on Image Processing*, 21(2):562–572, February 2012.

[4] Nicholas Chimitt and Stanley H. Chan. Simulating anisoplanatic turbulence by sampling correlated zernike coefficients. In *2020 IEEE International Conference on Computational Photography (ICCP)*, pages 1–12, Saint Louis, MO, USA, 24-26 April 2020.

[5] C-A. Deledalle and J. Gilles. Blind Atmospheric TUrbulence Deconvolution. *IET Image Processing*, 14(14):3422–3432, 2020.

[6] J.Gilles. Empirical Wavelet Transform. *IEEE Transactions on Signal Processing*, 61(16):3999–4010, 2013.

[7] J.Gilles. Continuous empirical wavelets systems. *Advances in Data Science and Adaptive Analysis*, 12(03n04):2050006, 2020.

[8] J.Gilles, F.Alvarez, N.B.Ferrante, M.Fortman, L.Tahir, A.Tarter, and A.von Seeger. Detection of moving objects through turbulent media. Decomposition of Oscillatory vs Non-Oscillatory spatio-temporal vector fields. *Image and Vision Computing Journal*, 73:40–55, 2018.

[9] J.Gilles, G.Tran, and S.Osher. 2d empirical transforms. wavelets, ridgelets and curvelets revisited. *SIAM Journal on Imaging Sciences*, 7(1):157–186, 2014.

[10] J.Gilles and K.Heal. A parameterless scale-space approach to find meaningful modes in histograms - application to image and spectrum segmentation. *International Journal of Wavelets, Multiresolution and Information Processing*, 12(6):1450044–1–1450044–17, 2014.

[11] J.Gilles and S.Osher. Fried deconvolution. In *SPIE Defense, Security and Sensing conference*, Baltimore, US, April 2012.

[12] Adam Kaufman and Raanan Fattal. Deblurring using analysis-synthesis networks pair. *CoRR*, abs/2004.02956, 2020.

[13] Orest Kupyn, Tetiana Martyniuk, Junru Wu, and Zhangyang Wang. Deblurgan-v2: Deblurring (orders-of-magnitude) faster and better. *CoRR*, abs/1908.03826, 2019.

[14] Yu Mao and Jérôme Gilles. Non rigid geometric distortions correction - application to atmospheric turbulence stabilization. *Journal of Inverse Problems and Imaging*, 6(3):531–546, 2012.

[15] Zhiyuan Mao, Nicholas Chimitt, and Stanley H. Chan. Image reconstruction of static and dynamic scenes through anisoplanatic turbulence. *IEEE Transactions on Computational Imaging*, 6:1415–1428, October 2020.

[16] Seungjun Nah, Tae Hyun Kim, and Kyoung Mu Lee. Deep multi-scale convolutional neural network for dynamic scene deblurring. *CoRR*, abs/1612.02177, 2016.

[17] N.Ferrante, S.Parameswaran, and J.Gilles. Investigation of moving objects through atmospheric turbulence from a non-stationary platform. In *Proceedings of the SPIE 11137, Applications of Digital Image Processing XLII*, San Diego, USA, August 2019.

[18] Jinshan Pan, Haoran Bai, and Jinhui Tang. Cascaded deep video deblurring using temporal sharpness prior. *CoRR*, abs/2004.02501, 2020.

[19] S.Parameswaran, C-A.Deledalle, L.Denis, and T.Q. Nguyen. Accelerating GMM-Based Patch Priors for Image Restoration: Three Ingredients for a 100$\times$ Speed-Up. *IEEE Transaction on Image Processing*, 28(2):687–698, 2019.

[20] Xin Tao, Hongyun Gao, Yi Wang, Xiaoyong Shen, Jue Wang, and Jiaya Jia. Scale-recurrent network for deep image deblurring. *CoRR*, abs/1802.01770, 2018.

[21] E. Tretiak, O. Barinova, P. Kohli, and V. Lempitsky. Geometric image parsing in man-made environments. *International Journal of Computer Vision*, 97:305–321, 2012.

[22] Emanuele Trucco and Alessandro Verri. *Introductory techniques for 3-D computer vision*, volume 201. Prentice Hall Englewood Cliffs, 1998.

[23] Haichao Zhang, David Wipf, and Yanning Zhang. Multi-image blind deblurring using a coupled adaptive sparse prior. In *2013 IEEE Conference on Computer Vision and Pattern Recognition*, Portland, OR, USA, June 2013. IEEE.